Journal of Neuroinflammation

RESEARCH

Open Access

Multiomics integrated analysis and experimental validation identify TLR4 and ALOX5 as oxidative stress-related biomarkers in intracranial aneurysms

Lvyin Luo[1,2], Xinlong Ma[1,2], Debin Kong[1,2], Yuxiang Dai[1,2], Tao Li[3], Han Yu[4], Jingzheng Liu[1,2], Maogui Li[1,2], Yangyang Xu[1,2], Guo Xiang[1,2], Zhimin Zhao[1,2], Weiying Zhong[1,2], Donghai Wang[1,2] and Yunyan Wang[1,2*]

Abstract

Background Intracranial aneurysm (IA) is a severe cerebrovascular disease, and effective gene therapy and drug interventions for its treatment are still lacking. Oxidative stress (OS) is closely associated with the IA, but the key regulatory genes involved are still unclear. Through multiomics analysis and experimental validation, we identified two diagnostic markers for IA associated with OS.

Methods In this study, we first analyzed the IA dataset GSE75436 and conducted a joint analysis of oxidative stress-related genes (ORGs). Differential analysis, functional enrichment analysis, immune infiltration, WGCNA, PPI, LASSO, and other methods were used to identify IA diagnostic markers related to OS. Next, the functions of TLR4 and ALOX5 expression in IA and their potential targeted therapeutic drugs were analyzed. We also performed single-cell sequencing of patient IA and control (superficial temporal artery, STA) tissues. 23,342 cells were captured from 2 IA and 3 STA samples obtained from our center. Cell clustering and annotation were conducted using R software to observe the distribution of TLR4 and ALOX5 expression in IAs. Finally, the expression of TLR4 and ALOX5 were validated in IA patients and in an elastase-induced mouse IA model using experiments such as WB and immunofluorescence.

Results Through bioinformatics analysis, we identified 16 key ORGs associated with IA pathogenesis. Further screening revealed that ALOX5 and TLR4 were highly expressed to activate a series of inflammatory responses and reduce the production of myocytes. Methotrexate (MTX) may be a potential targeted drug. Single-cell analysis revealed a notable increase in immune cells in the IA group, with ALOX5 and TLR4 primarily localized to monocytes/macrophages. Validation through patient samples and mouse models confirmed high expression of ALOX5 and TLR4 in IAs.

Conclusions Bioinformatics analysis indicated that ALOX5 and TLR4 are the most significant ORGs associated with the pathogenesis of IA. Single-cell sequencing and experiments revealed that the high expression of ALOX5 and TLR4 are closely related to IA. These two genes are promising new targets for IA therapy.

Keywords Intracranial aneurysm, Oxidative stress, Bioinformatics analysis, Single-cell sequencing, Mouse IA model

*Correspondence:
Yunyan Wang
wangyunyan@email.sdu.edu.cn
Full list of author information is available at the end of the article

Background

Intracranial aneurysm (IA) is a severe cerebrovascular disease with an incidence rate of 3–5% [1], but its pathogenesis remains unclear. A ruptured IA causing aneurysmal subarachnoid hemorrhage (aSAH), that is a devastating cerebrovascular disease with a mortality range of 8.3–66.7% [2]. Currently, conventional treatments include open surgery and intervention therapy, both of which carry risks related to their invasive natures [3]. It is preferable to seek treatment before rupture occurs to prevent serious consequences. Therefore, understanding the pathogenesis of IA and identifying targets for its prevention and treatment are crucial.

The principal pathological characteristics of IA include immune cell infiltration, inflammation, Oxidative stress (OS), and cellular apoptosis. Notably, OS and inflammation play pivotal roles within this context [4]. OS represents a pivotal imbalance between the production and eradication of free radicals, with a pronounced involvement of reactive oxygen species (ROS) [5]. ROS impair the generation of antioxidant enzymes, thereby attenuating nitric oxide (NO) activity, resulting in endothelial dysfunction, widespread vascular cell apoptosis, and various sequelae, including vascular smooth cells (VSMC) migration and proliferation [6]. Studies have shown that some inflammatory cytokines production and inflammatory pathways activation require the involvement of ROS, with excessive OS inciting vascular inflammation and augmenting the likelihood of vascular injury [7, 8]. Concurrently, immune cells in IA are strongly associated with OS; for example, neutrophils release peroxidase, while M1 macrophages secrete high concentrations of superoxide and reactive nitrogen to increase OS in tissues [7, 9]. In addition, free radicals orchestrate lipid peroxidation, thereby instigating atherosclerosis, hemodynamic aberrations, and hypertension, all of which are pivotal factors in the genesis of IA, underscoring the pivotal role of OS in IA pathogenesis [10]. However, the precise mechanisms underlying OS in IA remain elusive, and the specific OS-related genes (ORGs) intimately linked with IA remain undefined. Consequently, the prospective identification of IA-associated OS biomarkers holds promise for elucidating novel research ideas and molecular targets.

In this study, we conducted analyses using the GSE75436 dataset to comprehensively validate the functionality of ORGs in IA. Differential expression, enrichment, immune infiltration, Weighted Gene Co-expression Network analysis (WGCNA), Protein–Protein Interaction Networks (PPI), The Least Absolute Shrinkage and Selection Operator (LASSO) and calibration curve analyses were used to identify TLR4 and ALOX5 as key genes associated with OS in IA patients. The GSE15629 dataset was utilized for external validation, along with predictions of transcription factors (TFs), miRNAs, and small molecule drugs. Furthermore, single-cell sequencing of human IA was performed, incorporating 2 IA samples and 3 superficial temporal artery (STA) samples for merged analysis, to observe the distribution of TLR4 and ALOX5 in the single-cell data. Finally, the expression of TLR4 and ALOX5 was assessed in IA patients and an IA mouse model.

Materials and methods

Tissue sample collection

In this study, tissues from 2 patients with IA and 3 patients with STA who underwent aneurysm clipping surgery at Qilu Hospital of Shandong University were collected for single-cell sequencing. Tissues from 3 patients with IA and 3 patients with STA were subjected to paraffin sectioning (Additional file 1: Table S1). Detailed clinical information can be found in the supplementary files. The study was carried out in strict accordance with the principles of the Declaration of Helsinki. The protocol was reviewed and approved by the Ethics Committee of Qilu Hospital of Shandong University. Informed written consent was obtained from each patient who participated in the study.

Data obtain and processing

The gene expression profiles GSE75436 [11], GSE15629 [12], and GSE36791 [13] from the National Center for Biotechnology Information. Within GSE75436, 15 samples of aneurysm tissue were collected via neurosurgical clipping, along with 15 samples of STA tissue from patients. The use of the dataset can be found in (Additional file 1: Table S2). Furthermore, we acquired data on 467 genes related to OS (Additional file 2) from the Gene Ontology (GO) database (Gene Ontology Resource).

Identification of different expression genes (DEGs) and enrichment analysis

The DEGs were identified utilizing the "Limma" R package [14]. Genes meeting the screening criteria [|log2 FC (fold change) |> 1, $p < 0.05$] were deemed the cutoff for the DEGs. Enrichment analyses for DEGs were performed using the "clusterProfiler" R package (version 3.14.3) [15]. REVIGO is a web platform that uses GO terms from prior enrichment analyses for further visualization and interpretation of the results. It employs a clustering algorithm based on semantic similarity measures, offering several outputs to aid in the interpretation [16].

Evaluation of immune cell infiltration

Immune cell infiltration analysis and visualization were implemented with SangerBox 3.0 [17]. Based on the expression profiling of the GSE75436 dataset,

the CIBERSORT [18] and xCell algorithms [19] were employed to analyze the immune cells infiltration levels.

Construction of weighted gene coexpression networks

WGCNAs are used to describe gene association patterns between different samples, and can be used to identify candidate biomarker genes based on gene set connectivity and association between gene sets and phenotypes. The "goodSamplesGenes" method from the "WGCNA" R package was utilized to eliminate outlier genes. Subsequently, WGCNA was utilized to construct scale-free coexpression networks [20]. The optimal β value (β = 22) was determined for an R^2 value > 0.85. Within the candidate modules, genes with |Module Membership| (|MM|) > 0.8 and |Gene Significance| (|GS|) > 0.20 were filtered as key genes.

LASSO-cox regression and PPI network

LASSO regression is primarily used for variable selection and regularization in high-dimensional data. It selects key feature genes from high-dimensional gene expression data, thereby enhancing the predictive power of the model. The R package "glmnet" was employed for LASSO regression analysis [21]. Based on the expression profile data, the genes with the highest predicted values among the key genes were identified. PPI reveals biological processes within cells by studying the physical and functional interactions between proteins, and is used to understand disease mechanisms and identify potential drug targets. The PPI was constructed using STRING database [22]. The CytoHubba [23] plug-in within Cytoscape [24] was used to identify significant genes. MCC can be used to identify those nodes that have strong connectivity in the network and are part of many highly connected subgraphs. Such nodes often have important functions in the network. MNC measures the extent to which a node's neighbors form a connected component. As for Degree, degree centrality is one of the simplest and most intuitive measurements of network centrality. EcCentricity is often used to evaluate the central and edge nodes in the network, which can help understand the network structure and information propagation path.

External validation

The GSE15629 and GSE36791 datasets were used as external validation datasets. The "pROC" R package was utilized for receiver operating characteristic (ROC) curve construction. Calculate the area under the curve (AUC) values to compare the predictive efficiency of candidate genes in distinguishing between IA and control samples. An AUC > 0.7 was considered indicative of good predictive performance.

Gene set enrichment analysis (GSEA)

GSEA was used to identify the potential functions of the diagnostic genes [25]. For single-gene GSEA (sg-GSEA), the selected reference gene set was downloaded from the Molecular Signature Database (MSigDB) [26]. Based on the expression levels of genes, the samples were divided into a high-expression group (≥ 50%) and a low-expression group (< 50%). We retrieved the genes to assess relevant pathways and molecular mechanisms. Our analysis utilized a minimum gene set size of 5 and a maximum gene set size of 5000, with 1000 resamplings. |NES| (normalized enrichment score) > 1 was considered significant, and $p < 0.05$ was considered to indicate statistical significance.

Potential TF and miRNA–target gene regulatory networks were constructed and small-molecule drug prediction

The miRNet online database (https://www.mirnet.ca/) was utilized to identify potential miRNAs targeting diagnostic genes [16]. The TFs were predicted using NetworkAnalyst (https://www.networkanalyst.ca/) [27]. Small-molecule drugs were searched using the gene names in the DGIdb database (https://dgidb.org) [28].

Single-cell sequencing and analysis

Samples obtained in the operating room were rapidly placed in precooled sterile PBS to wash away adherent red blood cells on the vessel walls, transferred to specialized tissue preservation solution and transported to the laboratory on ice. Tissues were washed and lysed in mixed digestion buffer. The samples were digested on a 37 °C shaker for 1 h, followed by filtration through a 40 μm filter and centrifugation at 300 × g for 5 min. After removing the supernatant, the cells were gently dispersed in red blood cell lysis buffer and incubated for 3 min, after which the lysis was terminated by the addition of wash buffer. After centrifugation, the cells were resuspended and thoroughly mixed in wash buffer to obtain a single-cell suspension.

The BD Rhapsody WTA Analysis Pipeline was used to construct sequencing libraries from single-cell transcriptomes. The analysis pipeline performed sequence alignment using FASTQ files, reference genome files (human: GRch38), and transcriptome annotation files (human: GENCODE v32/Ensembl 98). Fastq files exported from sequencing were processed using the Cell Ranger Single-Cell Software. Batch effect removal was carried out as part of the Cell Ranger sorting protocol. Downstream analysis of the matrix files was performed using the Seurat R package (version 4.3.01). Low-quality cells were filtered according to a set of criteria (200 < nFeature RNA < 6000 & nCount_RNA < 50000 & percent.mt < 30),

and the dataset was normalized and log-transformed. Identification of cell clusters is performed using the FindClusters function, (resolution = 0.5). Unsupervised clustering and dot plots were used to visualize cell markers for each cluster, followed by manual annotation.

Construction of the mouse IA model

The animal experiments were conducted following the protocol approved by the Animal Ethics Committee of Qilu Hospital, Shandong University, and followed the "3R" principle to minimize animal suffering. We constructed a mouse IA model using a previously described elastase-induced method [29, 30]. Briefly, 6–8 week-old male C57BL/6 J mice were subjected to left renal artery ligation and left carotid artery ligation under abdominal anesthesia with tribromoethanol, accompanied by administration of a high-salt diet (8% NaCl). One week later, with the assistance of a stereotaxic apparatus, a cranial drill was used to create a hole, and elastase solution was injected into the basal cistern. After 4 weeks of feeding, the mice were euthanized, and their hearts were perfused with prewarmed gelatin-trypan blue solution. Subsequently, the mice were placed in ice for 5 min to cast the cerebral vessels. The morphology of cerebral vessels in the circle of Willis was observed under a microscope. Blood vessels were then extracted and stored for future use.

Western blot, immunohistochemistry (IHC) and immunofluorescence (IF)

Protein immunoblotting and IHC were performed according to previously described methods [31]. The following antibodies were used for immunoblotting: mouse anti-TLR4 (1:1000, Proteintech), rabbit anti-ALOX5 (1:1000, Boster), and rabbit anti-β-actin (1:1000, Huabio). The following antibodies were used for IHC: mouse anti-TLR4 (1:50, Proteintech) and rabbit anti-ALOX5 (1:50, ABclonal). For IF double staining, the paraffin mouse brain tissue and human brain vessel sections were incubated with a mixture of mouse anti-TLR4 (1:50, Proteintech) and rabbit anti-ALOX5 (1:50, ABclonal) primary antibodies. Subsequently, the following secondary antibodies were incubated with the sections: CY3-labeled goat anti-mouse IgG (1:300, Servicebio) and Alexa Fluor 488-labeled goat anti-rabbit IgG (1:300, Beyotime). Imaging was performed using a laser confocal microscope (Leica, Wetzlar, Germany).

Statistical analysis

Statistical analysis was conducted using GraphPad Prism (version 9.0). Some of the statistics were automated by R software (version 4.3.1). Unless otherwise specified, the analysis in R is run with default parameters. The statistical results of the immune infiltration and correlation analysis are done by the default parameters of the SangerBox. Quantitative analysis of protein immunoblotting and immunohistochemistry data was performed using ImageJ software (version 1.5.3) (NIH, MD, USA). The obtained grayscale values and mean absorbance values were imported into GraphPad software for analysis via the independent samples t test method, and the results are presented as the means ± standard deviations (means ± SDs). $P < 0.05$ was considered to indicate statistical significance.

Results

Identification and enrichment analysis of ORGs in IA

Differential expression analysis was conducted on the GSE75436 dataset using the Limma method, revealing significant differences between the IA and STA groups. Compared to those in the STA group, 1315 upregulated genes and 1127 with downregulated genes were identified in the IA group (Fig. 1A, B). The intersection of DEGs with ORGs revealed 63 DEORGs (Fig. 1C). A list of differential genes can be found in Additional file 3.

Functional analysis of DEORGs was performed using multiple gene sets. GO analysis was performed separately on the upregulated and downregulated DEORGs, with redundant terms removed using the REVIGO website. The results showed that both the upregulated and downregulated DEORGs were mainly enriched in the Biological Process (BP) terms of response to stress, response to oxidative stress, and response to chemical. However, they differed in the Cellular Component (CC) and Molecular Function (MF) categories (Fig. 1D, E). KEGG analysis revealed enrichment of these genes in pathways such as malaria, arachidonic acid metabolism, and toxoplasmosis (Fig. 1F). Hallmark pathway enrichment analysis revealed close associations between DEORGs and pathways such as apoptosis, IL-6/JAK/STAT3 signaling, and myogenesis (Fig. 1G). The enrichment results can be found in Additional file 4.

Immune infiltration and WGCNA

To explore the relationship between immunity and IA formation, we constructed a landscape of GSE75436 immune infiltration data (Fig. 2A). We analyzed the percentages of different immune cells in the CIBERSORT algorithm in both IA and Control tissues, and the results showed that M2 macrophages were well represented in both the IA and Control groups, and that there were more in the IA group. In addition, mast resting cells and T_Cells_gamma_delta were the most common in IA, and neutrophils and T_Cells_gamma_delta were the most common in control (Fig. 2B). Five types of immune cells showed significant differences in abundance between the

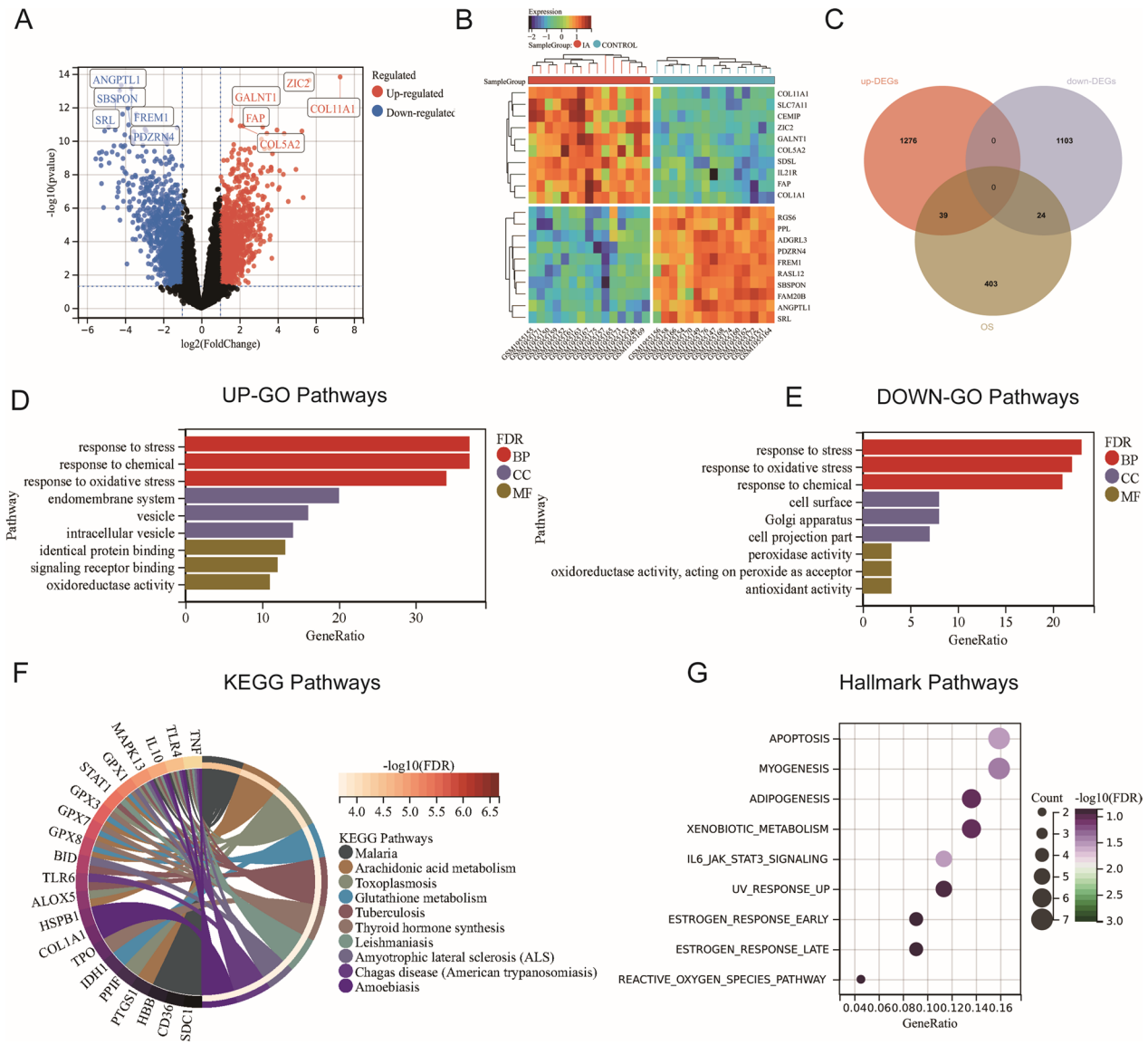

Fig. 1 Identification and enrichment analysis of ORGs. **A** Volcano plot of DEGs in the GSE75436 dataset, with filtering criteria of |log2FC|> 1 and p < 0.05. **B** Heatmap showing the top ten genes with upregulated or downregulated expression. **C** Identification of 63 DEGs related to OS. **D**, **E** GO analysis of DEGs. **F** Chordal diagram about KEGG analysis. **G** Hallmark pathway analysis

IA and control samples (p < 0.05). These included naïve CD4 + T-cells, monocytes, M1 macrophages, and resting and activated mast cells (Fig. 2C). The xCell algorithm was used to calculate the xCell score through transcriptomic data to analyze the immune microenvironment. The immune score, stroma score, and microenvironment score were significantly different between IA tissues and normal tissues (Fig. 2D). The immunization score is provided in Additional file 5: Table S5.

For WGCNA, The optimal soft threshold power (β = 22) was chosen according to the construction of a scale-free network (Fig. 2E). We identified 10 coexpression modules from 30 samples of 20,020 genes, which are shown in different colors (Fig. 2F). Subsequently, we analyzed the correlation between the module and immune-infiltrating cells by Pearson correlation analysis and found that the pink module was most strongly correlated with resting mast cells (Cor = 0.63, P = 2.2e − 4) and that the light green module was strongly correlated with M2 macrophages (Cor = 0.62, P = 2.3e − 4) (Fig. 2G). Significant correlations between GS (Gene Significance) and MM (Module Membership) are showcased within the pink and light green modules (Fig. 2H). As a result, these modules, associated with immune infiltrating cells, were

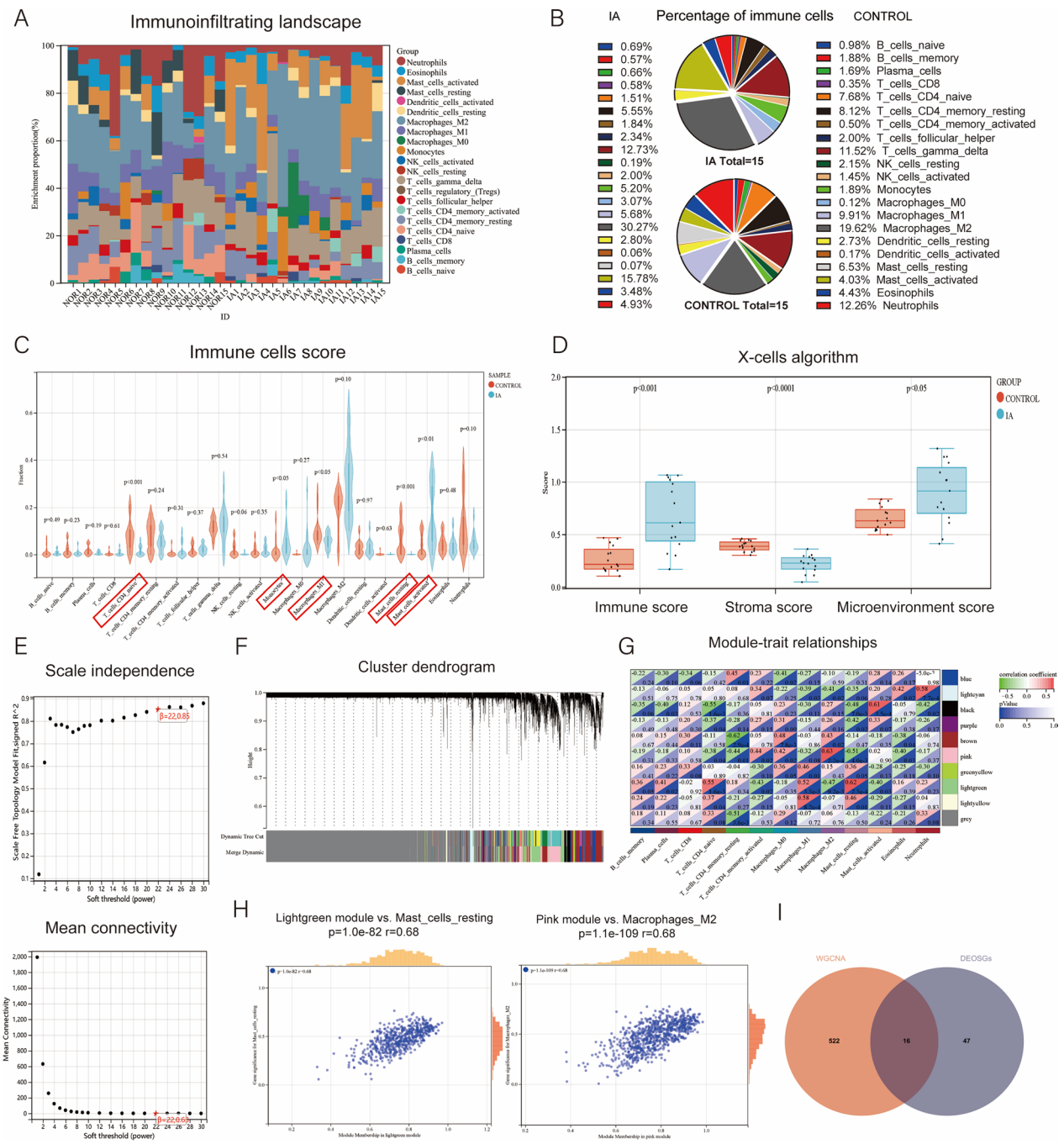

Fig. 2 Immunoinfiltration analysis and WGCNA revealed the role of immune cells in IA. **A** Immunoinfiltration landscape in the GSE75436 dataset. **B** Percentage of immune cells in IA. **C** Abundance levels of various immune cells in the IA and control groups. **D** Immune scores, stromal scores, and microenvironment scores derived from the xCell algorithm. **E** Selection of the optimal soft-thresholding power (β). **F** Identification of 10 modules presented as a clustering tree. **G** Correlations between modules and immune cells. **H** The correlation between the light green module and Mast_cells_resting, and the correlation between the pink module and M2 macrophages. **I** Extraction of 538 hub genes from the light green and pink modules intersecting with DEORGs, resulting in 16 key genes

deemed pivotal and earmarked for further scrutiny. The hubgenes for the two modules are found in Additional file 6. A sum of 538 hub genes, exhibiting GS values exceeding 0.20 and MM values surpassing 0.80, were culled from these modules for subsequent analysis. We intersected these genes with the DEORGs and identified

16 hub genes: CRYAB, KCNA5, MSRB2, TLR4, AIF1, BID, APOE, TREM2, HMOX1, RBPMS, TLR6, MAPK13, ALOX5, CD38, BTK and GPX1 (Fig. 2I).

Further screening of hub genes and identification of their functions

We analyzed the correlations among these 16 hub genes (Fig. 3A) and generally found a strong correlation among them. Subsequently, we explored the PPIs of these 16 DEORGs (Fig. 3B). MCC algorithm in the CytoHubba plugin to was employed to evaluate these interacting proteins, with the top six being TLR4, APOE, AIF1, HMOX1, ALOX5, and TRPM2 (Fig. 3C). Additionally, we used various algorithms, including MNC, degree, and EcCentricity, to assess hub genes. These scores can be found in Additional file 7.

Next, LASSO analysis was performed on these 16 genes, with an ideal lambda value set at 0.1475, resulting

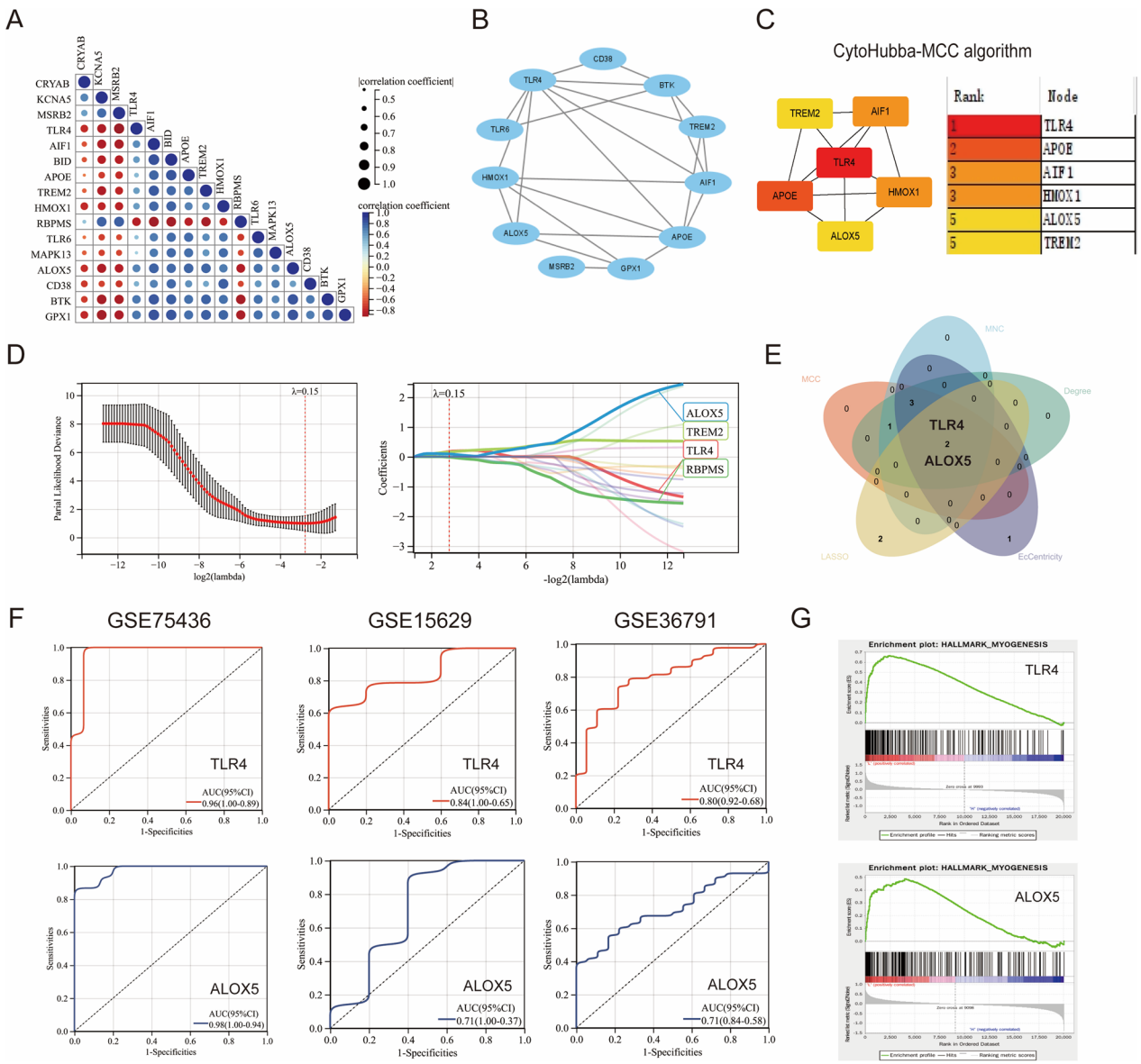

Fig. 3 Further validation, external verification, and functional analysis of hub genes. **A** Correlations among the 16 hub genes. **B** Using was Cytoscape software to construct A PPI network. **C** Score of MCC algorithm in CytoHubba. **D** Determination of the soft-thresholding power (lambda = 0.15) and selection 4 genes through LASSO analysis. **E** The Venn diagram illustrates the intersection of LASSO with various PPI algorithms. **F** ROC curve of TLR4 and ALOX5 in the GSE75436 dataset and the external validation dataset. An AUC > 0.7 was considered to indicate good predictive performance. **G** In GSE75436, TLR4 and ALOX5 low expression groups were enriched in the myogenesis pathway

in the identification of 4 genes, ALOX5, TREM2, TLR4, and RBPMS (Fig. 3D). LASSO results can be found in Additional file 8. The results of LASSO-Cox were consistent with the PPI algorithms, revealing 2 hub genes, namely, TLR4 and ALOX5 (Fig. 3E). These two genes may be key genes involved in the pathogenesis of IA. Next, we validated their predictive ability.

We performed internal and external dataset validation of the hub genes employing ROC curves to evaluate their diagnostic precision (Fig. 3F). In GSE75436, the AUC for TLR4 was 0.96, and that for ALOX5 was 0.98. GSE15629 is a dataset containing data on 14 patients with IA and 5 controls, with AUCs of 0.84 and 0.71 for TLR4 and ALOX5, respectively. We also unexpectedly found that TLR4 and ALOX5 exhibited good predictive performance in the GSE36791 dataset, with AUCs of 0.80 and 0.71, respectively. GSE36791 is a serum dataset containing data on 43 patients with ruptured IA and 18 controls, suggesting that these two hub genes may also have diagnostic effects on ruptured aneurysms. Sg-GSEA shows the impact of TLR4 and ALOX5 expression levels on IA modulation. Low TLR4 and ALOX5 expression was enriched in the myogenic pathway. (Fig. 3G). Sg-GSEA results can be attached in Additional file 9.

Exploring miRNA regulatory networks and potential small molecule drugs

We used online websites to predict the upstream TFs, interacting miRNAs, and potential targeted drugs for TLR4 and ALOX5. Among them, EGR1, SP1, HDAC2, and TP53 are TFs that can regulate ALOX5, while ZNF160, IRF3, and IRF8 are TFs that can regulate TLR4. There was no overlap in the TFs regulating each gene. For small-molecule drugs, resatorvid and eritoran tetrasodium are the most highly scored TLR4 inhibitors, while diethylcarbamazine and zileuton are the most strongly scored ALOX5 inhibitors. Methotrexate (MTX) is a common inhibitor of both genes and may have potential therapeutic effects. miRNAs such as hsa-miR-146a-5p and hsa-let-7d-5p coregulate ALOX5 and TLR4 (Additional file 1:Fig. S1A-D). TF, miRNA network and drug results can be found in Additional files 10 and 11.

scRNA-seq analysis

Two IA samples and 3 STA samples were subjected to single-cell sequencing. After screening based on the quality control criteria described in the methods, 23,342 cells were selected. After the samples were merged, 20 different cell clusters were identified by unsupervised Seurat clustering (Fig. 4A). Based on the expression levels of typical cell type-specific markers, dot plots were drawn, and the cells were manually annotated (Fig. 4B), including VSMCs (MYH11, ACTA2, MYL9, and TAGLN), T- and NK cells (NKTR, CD3E, TRAC, and TRBC2), Mos/Mϕs (CSF1R and CD14), neutrophils (S100A9, CSF3R, and FCGR3B), DCs (CD74, IRF8, and HLA-DRA), endothelial cells (PECAM1, VWF, and FLT1), fibroblasts (DCN, PDGFRA), Schwann cells (MPZ, PLP1, and PMP22), and mast cells (MS4A2). The cell clusters were ultimately classified into 9 types, and UMAP was used to display the cell distribution (Fig. 4C). Groupwise analysis revealed an obvious increase in the numbers of immune cells such as T- and NK cells, neutrophils, and Mos/Mϕs in the IA group. Mapping ALOX5 and TLR4 expression onto the UMAP plot revealed that they were mainly distributed in the Mo/Mϕ cluster and neutrophil cluster of the IA group (Fig. 4D). We further visualized the expression of these two hub genes in various cell clusters using violin plots and dot plots. The average expression level of ALOX5 was 1.93 in mast cells and 1.05 in neutrophil clusters, significantly higher than in VSMC clusters (−0.75), fibroblast clusters (−0.76), and endothelial cell clusters (−0.74). For TLR4, the average expression level was 2.12 in neutrophil clusters and 1.18 in Mo/Mϕ clusters, significantly higher than in VSMC clusters (−0.64) and fibroblast clusters (−0.52) (Fig. 4E, F).

Expression of ALOX5 and TLR4 in IA patients and elastase-treated IA mice

To validate the expression of the hub genes ALOX5 and TLR4 in IA patient tissues, we performed IHC and IF staining on IA samples and STA samples, which were used as controls. TLR4 and ALOX5 expression were mainly distributed in the cytoplasm, and their average optical density (AOD) in IA tissues was significantly greater than that in control tissues ($p < 0.05$, Fig. 5A, B). In addition, IF staining revealed a notable increase in the number of cells positive for TLR4 and ALOX5 expression in the IA tissues (Fig. 5C).

We used elastase induction combined with hypertension to construct a mouse IA model (Fig. 6A). Microscopic observation of mouse Willis' ring morphology revealed local protrusions in blood vessels, which is indicative of aneurysm formation (Fig. 6B). Compared with that in control brain vessels, IF staining revealed a significant increase in the expression of TLR4 and ALOX5 at IA sites (Fig. 6C). Subsequently, brain vessels from the Willis' rings of the mice were extracted for WB detection, and the results showed a significant increase in the protein expression levels of TLR4 and ALOX5 in the IA group ($p < 0.05$, Fig. 6D, E).

Discussion

The development of IA involves multiple biological processes, with evidence highlighting the critical roles of OS and inflammation [4]. OS and inflammation interact

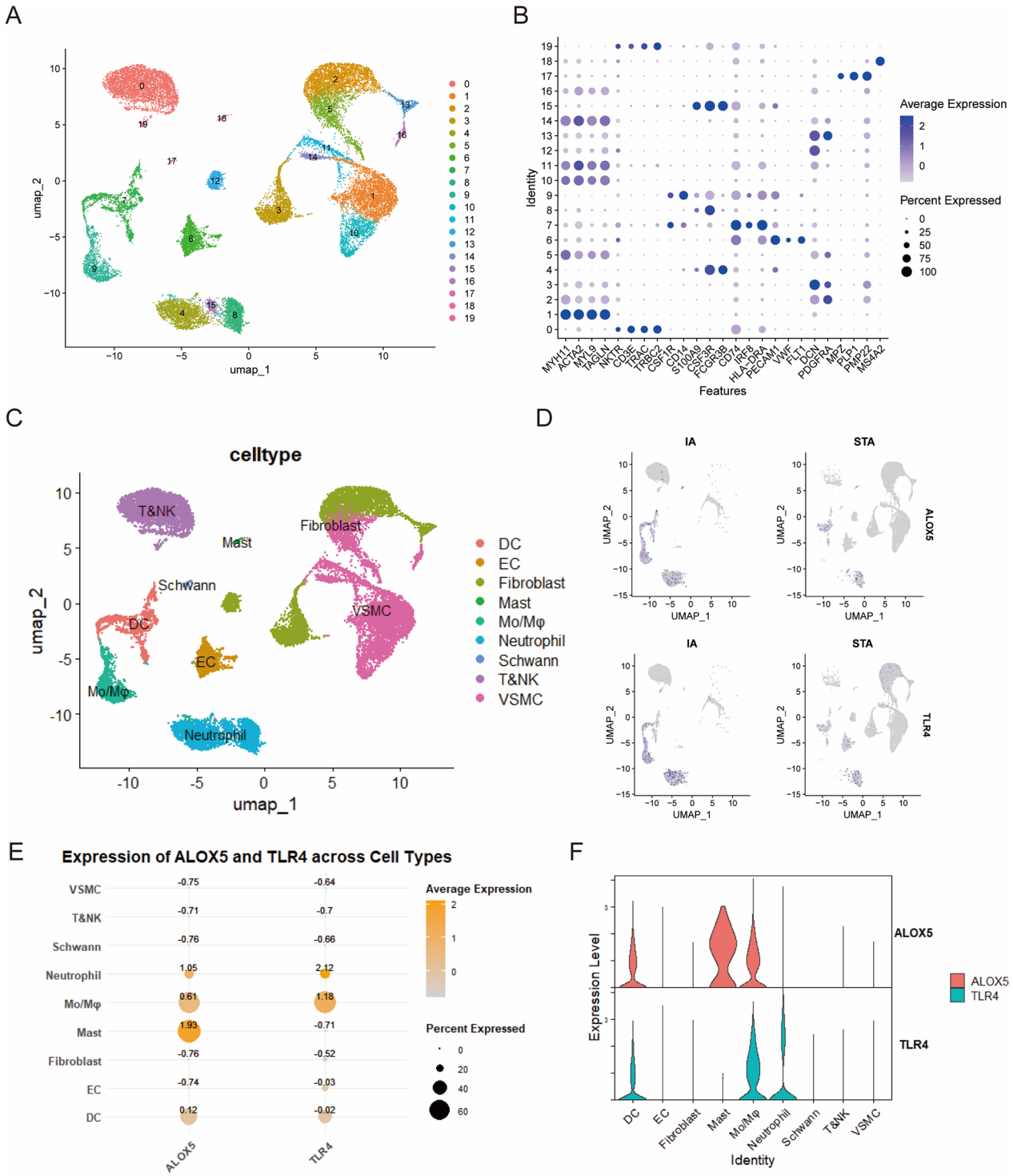

Fig. 4 scRNA-seq analysis of TLR4 and ALOX5 expression in patient IA. **A** UMAP visualization of 20 clusters identified through unsupervised clustering. **B** Dot plot of characteristic marker genes used for cell type identification. **C** UMAP showing annotated cells. **D** Groupwise expression of TLR4 and ALOX5 in the IA and STA groups. **E** Dot plot showing the expression of TLR4 and ALOX5 in each cell cluster. **F** Violin plot showing the expression of TLR4 and ALOX5 in different cells

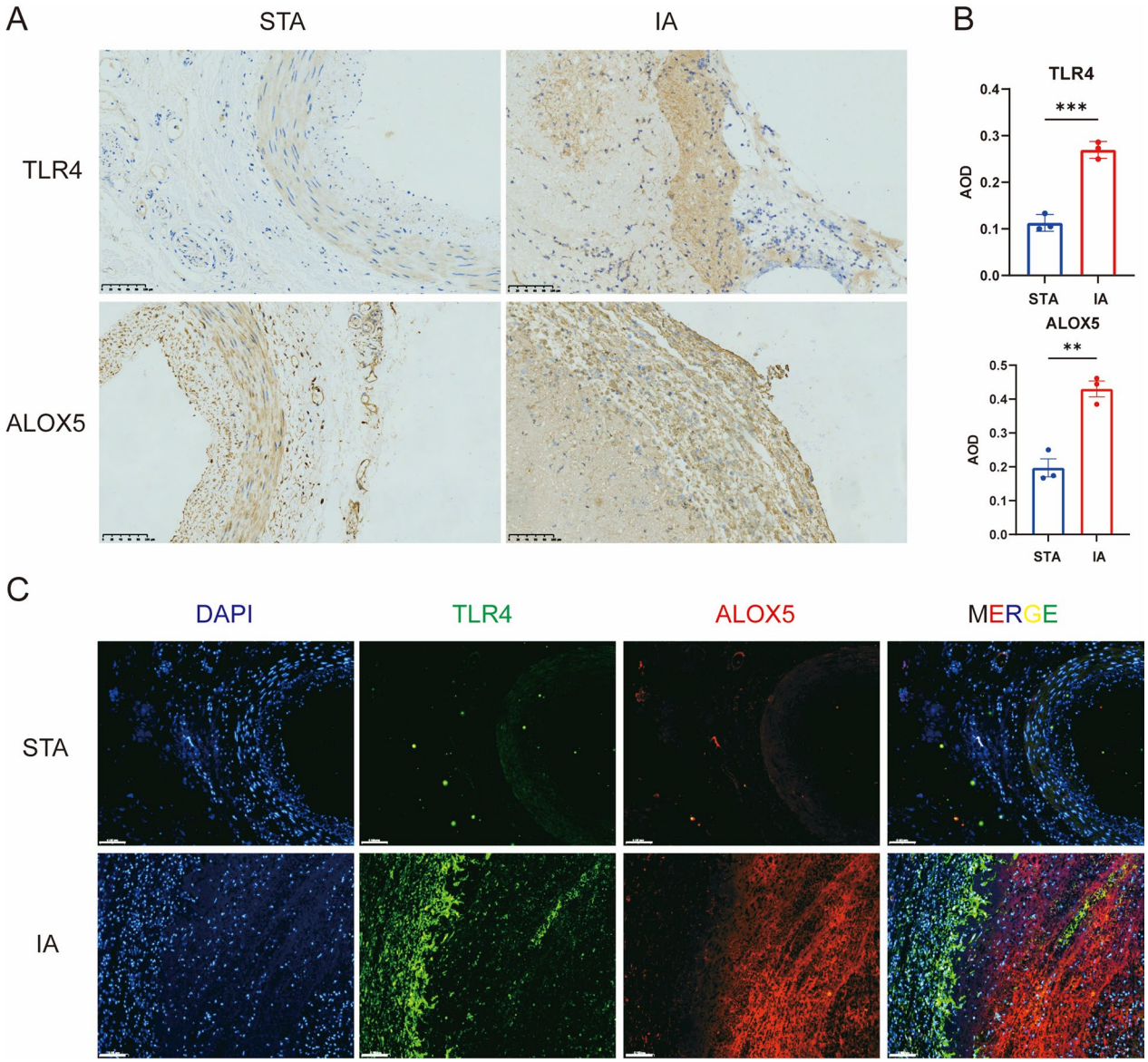

Fig. 5 Validation of hub gene expression in patients. **A** Immunohistochemical validation of TLR4 and ALOX5 expression in the IA and STA groups. (Scale bar: 100 μm). **B** Statistical analysis of the AOD of TLR4 and ALOX5 expression. **C** Immunofluorescence of TLR4 and ALOX5 expression (scale bar: 100 μm). $^{**}p < 0.01$; $^{***}p < 0.001$

through ROS, leading to endothelial damage and matrix remodeling, which may promote IA formation and rupture [10, 32]. However, it is still unclear which genes play important regulatory roles in this process. Discovering new and efficacious biomarkers is crucial.

In this study, we identified 63 DEORGs in the GSE75436 dataset, enriched in functions like oxidative stress, apoptosis, and IL-6/JAK/STAT3 signaling. ROS from damaged mitochondria in arterial walls contribute to IA by disrupting vascular homeostasis [33]. Recent analyses also link mitochondrial dysfunction-related genes with ROS in IA [34], with IL-6/JAK/STAT3 signaling implicated in IA occurrence [35]. Next, immune infiltration analysis showed increased activated mast cells, monocytes, and macrophages in IA. Mast cells involvement in the progress of vascular diseases by secreting matrix metalloproteinases (MMPs) and elastases [36] and play significant roles in microbial defense and allergies [37]. Additionally, Monocytes and macrophages are considered key inflammatory components infiltrating the IA wall [38]. Unexpectedly, our findings revealed a higher in M2/M1 macrophage ratio the IA group,

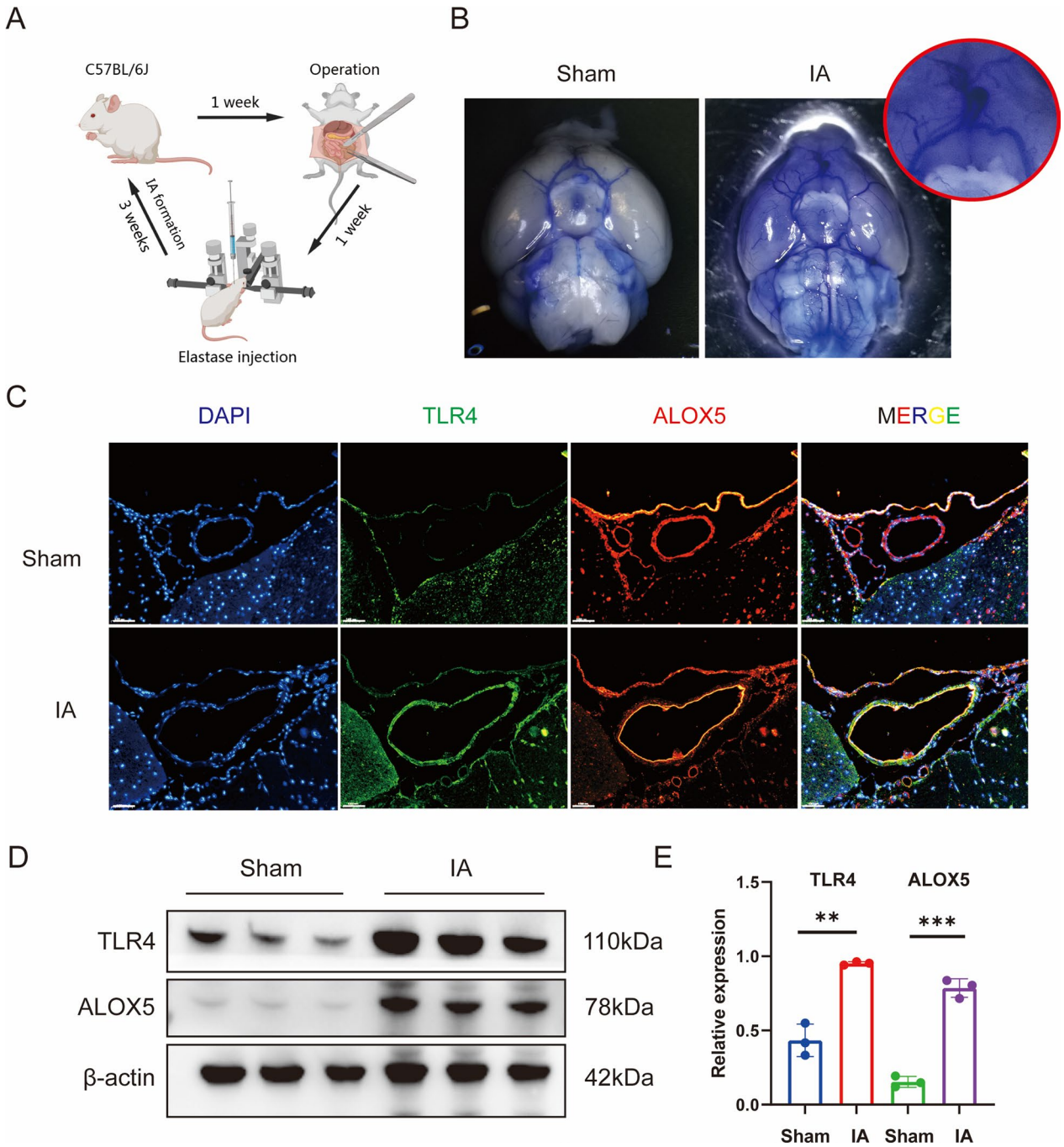

Fig. 6 Validation of TLR4 and ALOX5 expression in the mouse IA model. **A** Model construction process. **B** Typical images of aneurysm formation in the Willis' rings observed under a microscope. **C** Immunofluorescence validation of TLR4 and ALOX5 expression in IA tissues (scale bar: 50 μm). **D** WB analysis of TLR4 and ALOX5 protein expression (n = 3/per group). **E** Statistical analysis of grayscale values. $^{**}p < 0.01$; $^{***}p < 0.001$

potentially stabilizing unruptured aneurysms [31, 39]. Previous research has indicated that the imbalance in the M1/M2 macrophage ratio in IA leading to aneurysm rupture is related to the number of mast cells and is the result of interactions among multiple immune cells [40]. To further explore the role of immune cells in IA development, we performed sc-RNA seq analysis. Sc-RNAseq results corroborated this viewpoint; during the occurrence of IA, there was a significant loss of muscle cells and substantial recruitment of immune cells such as

Mos/Mφs, mast cells, and neutrophils. Using immune cells as features for WGCNA, we selected 16 candidate ORGs. We performed LASSO Cox analysis on these 16 genes and constructed a PPI network, ultimately identified TLR4 and ALOX5 as key DEORGs in IA.

TLR4 is a Toll-like receptor which expressed on immune and vascular cells, consisting of three distinct parts [41, 42]. Upon activation, TLR4 triggers the MyD88-dependent pathway and the TRIF-dependent pathway. Both pathways induce the expression of numerous proinflammatory factors, including interleukin-1β (IL-1β) and tumor necrosis factor-α (TNF-α) [43–45]. TLR4 mainly expressed in the endothelial cell layer of the IA wall and is in a transient unregulated state in the early stages of cerebral aneurysm formation. The expression of TLR4 demonstrates a strong correlation with NF-κB activation, indicating a potentially pivotal role for this receptor in the formation of cerebral aneurysms via NF-κB activation within endothelial cells [46, 47]. Moreover, a lack of TLR4 expression reduces the levels of inflammatory cytokines in cerebral arteries. Knocking out TLR4 expression reduces the rupture rate of mouse IAs [48].

ALOX5, involved in lipid peroxidation and ferroptosis, is linked to cardiovascular diseases [49]. Polymorphisms in ALOX5 increase atherosclerosis and myocardial infarction risk [50]. ALOX5 expression may regulate macrophage ferroptosis, promoting atherosclerosis [51, 52]. An extensive RNA-seq analysis unveiled a notable upsurge in ALOX5 expression among patients with IA [53]. Internal and external dataset validation demonstrated the good predictive performance of TLR4 and ALOX5. We validated this finding using a mouse IA model and clinical IA samples and found high expression of TLR4 and ALOX5 in IA tissues, consistent with our analytical results.

We further explored the functions of TLR4 and ALOX5. Single-gene GSEA showed that high expression of both TLR4 and ALOX5 was accompanied by downregulation of activity of the myogenesis pathway, which is consistent with the pathological features of IA [54]. Single-cell data revealed that TLR4 and ALOX5 were highly expressed in Mos/Mφs, mast cells, dendritic cells, and neutrophils in IA, which also confirms our results. We also constructed regulatory networks of TFs, miRNAs, and small molecule drugs and found that MTX is a targeted drug that acts on both ALOX5 and TLR4. Shen et al. demonstrated through microRNA disease network analysis and in vivo experiments that low-dose oral administration of MTX has a therapeutic effect on abdominal aortic aneurysm (AAA) [55]. The findings from this study imply that MTX could serve as a promising therapeutic agent for treating IA, but more in vivo experiments are needed for validation.

In summary, we identified TLR4 and ALOX5 as key OS-related biomarkers in IA. Their high expression levels, particularly in immune cells, were validated through multiple datasets and a mouse model. These findings suggest that TLR4 and ALOX5 could be promising therapeutic targets for IA, warranting further investigation into their specific regulatory mechanisms and potential clinical applications. However, the study's reliance on a single dataset and limited sample size calls for additional validation in larger cohorts. Future research should also explore other potential biomarkers and their roles in IA pathogenesis.

Supplementary Information

The online version contains supplementary material available at https://doi.org/10.1186/s12974-024-03226-0.

Supplementary material 1.
Supplementary material 2.
Supplementary material 3.
Supplementary material 4.
Supplementary material 5.
Supplementary material 6.
Supplementary material 7.
Supplementary material 8.
Supplementary material 9.
Supplementary material 10.
Supplementary material 11.

Acknowledgements
Thanks for the editing service provided by Nature Research Editing Service.

Author contributions
LL and YW conceived and designed the study. LL and XM acquired the data and conducted bioinformatics analysis. LL, DK, and YD drafted the manuscript. LL, XM, DK, and YD participated in the construction of the animal model and immunohistochemical analysis. HY performed the western blot experiments. GX and ZZ were responsible for animal care and immunofluorescence imaging. TL, WZ, and DW reviewed, supervised, and edited the manuscript. ML, YX, and JL collected samples and clinical information from IA patients. YW provided funding and conducted scientific review. All authors have read and agreed to the publication version of the manuscript, consenting to take individual responsibility for their contributions and ensuring the accuracy or completeness of any questions related to any part of the work. All authors have read and approved the final manuscript.

Funding
This work was supported by the Natural Science Foundation of Shandong Province (ZR2022MH263), China Foundation for International Science Exchange (Z2018LSD001) and Qilu Zhongke New Kinetic Energy Innovation Research Institute (6010123142).

Availability of data and materials
The publicly available GSE datasets supporting the findings of this study can be found in the GEO database (https://www.ncbi.nlm.nih.gov/geo/). The data accession identifiers are as follows: GSE75436, GSE15629, and GSE36791. The scRNA-seq data provided in this study are deposited in the National Genomics Data Center, China National GeneBank Sequence Archive (GSA for Human) repository, with accession number HRA007438. Relevant data will be available from the corresponding author upon reasonable request.

Declarations

Ethics approval and consent to participate

This research protocol was conducted in accordance with the ethical principles of the Declaration of Helsinki and approved by the Ethics Committee of Qilu Hospital, Shandong University (KYLL-2024(ZM)-428). All patients and their guardians were informed about the use of the tissue and informed consent was provided. Animal experiments were performed according to the Guidelines for the Care and Use of Laboratory Animals (National Research Council (USA) Committee for the Updating of Guidelines for the Care and Use of Laboratory Animals, 2011) and approved by the Laboratory Animal Ethics Committee of Qilu Hospital, Shandong University (DWLL-2022-095). We strictly follow the "3R" principle and make every effort to minimize the suffering of animals and reduce the number of animals used.

Competing interests

The authors declare no competing interests.

Author details

[1]Department of Neurosurgery, Qilu Hospital, Cheeloo College of Medicine and Institute of Brain and Brain-Inspired Science, Shandong University, Jinan 250012, China. [2]Shandong Key Laboratory of Brain Function Remodeling, Jinan, China. [3]Department of Neurosurgery, the Third Affiliated Hospital of Shandong First Medical University, Jinan, China. [4]Department of Ophthalmology, Qilu Hospital, Shandong University, Jinan, China.

Received: 14 May 2024 Accepted: 6 September 2024
Published online: 15 September 2024

References

1. Morel S, Bijlenga P, Kwak BR. Intracranial aneurysm wall (in) stability–current state of knowledge and clinical perspectives. Neurosurg Rev. 2022;45(2):1233–53.
2. Macdonald RL, Schweizer TA. Spontaneous subarachnoid haemorrhage. Lancet. 2017;389(10069):655–66.
3. Etminan N, Rinkel GJ. Unruptured intracranial aneurysms: development, rupture and preventive management. Nat Rev Neurol. 2017;13(2):126.
4. Starke RM, et al. The role of oxidative stress in cerebral aneurysm formation and rupture. Curr Neurovasc Res. 2013;10(3):247–55.
5. Šćepanović V, et al. The role of oxidative stress as a risk factor for rupture of posterior inferior cerebellar artery aneurysms. Mol Biol Rep. 2018;45(6):2157–65.
6. Sheinberg DL, et al. Endothelial dysfunction in cerebral aneurysms. Neurosurg Focus. 2019;47(1):E3.
7. Hosaka K, Hoh BL. Inflammation and cerebral Aneurysms. Transl Stroke Res. 2014;5(2):190–8.
8. Lindsay TF, et al. Ruptured abdominal aortic aneurysm, a "two-hit" ischemia/reperfusion injury: evidence from an analysis of oxidative products. J Vasc Surg. 1999;30(2):219–28.
9. Sindrilaru A, et al. An unrestrained proinflammatory M1 macrophage population induced by iron impairs wound healing in humans and mice. J Clin Invest. 2011;121(3):985–97.
10. Papaharalambus CA, Griendling KK. Basic mechanisms of oxidative stress and reactive oxygen species in cardiovascular injury. Trends Cardiovasc Med. 2007;17(2):48–54.
11. Wang W, et al. Aberrant expression of lncRNAs and mRNAs in patients with intracranial aneurysm. Oncotarget. 2017;8(2):2477.
12. Pera J, et al. Gene expression profiles in human ruptured and unruptured intracranial aneurysms: what is the role of inflammation? Stroke. 2010;41(2):224–31.
13. Pera J, et al. Gene expression profiling of blood in ruptured intracranial aneurysms: in search of biomarkers. J Cereb Blood Flow Metab. 2013;33(7):1025–31.
14. Ritchie ME, et al. limma powers differential expression analyses for RNA-sequencing and microarray studies. Nucleic Acids Res. 2015;43(7):e47.
15. Yu G, et al. clusterProfiler: an R package for comparing biological themes among gene clusters. OMICS. 2012;16(5):284–7.
16. Chang L, et al. miRNet 2.0: network-based visual analytics for miRNA functional analysis and systems biology. Nucleic Acids Res. 2020;48(W1):W244-w251.
17. Shen W, et al. Sangerbox: a comprehensive, interaction-friendly clinical bioinformatics analysis platform. iMeta. 2022;1(3):e36.
18. Newman AM, et al. Robust enumeration of cell subsets from tissue expression profiles. Nat Methods. 2015;12(5):453–7.
19. Aran D, Hu Z, Butte AJ. xCell: digitally portraying the tissue cellular heterogeneity landscape. Genome Biol. 2017;18(1):220.
20. Langfelder P, Horvath S. WGCNA: an R package for weighted correlation network analysis. BMC Bioinform. 2008;9(1):559.
21. Tibshirani R. The lasso method for variable selection in the Cox model. Stat Med. 1997;16(4):385–95.
22. Szklarczyk D, et al. STRING v10: protein–protein interaction networks, integrated over the tree of life. Nucleic Acids Res. 2014;43(D1):D447–52.
23. Chin CH, et al. cytoHubba: identifying hub objects and sub-networks from complex interactome. BMC Syst Biol. 2014;8:S11.
24. Shannon P, et al. Cytoscape: a software environment for integrated models of biomolecular interaction networks. Genome Res. 2003;13(11):2498–504.
25. Subramanian A, et al. Gene set enrichment analysis: a knowledge-based approach for interpreting genome-wide expression profiles. Proc Natl Acad Sci U S A. 2005;102(43):15545–50.
26. Liberzon A, et al. The Molecular Signatures Database (MSigDB) hallmark gene set collection. Cell Syst. 2015;1(6):417–25.
27. Zhou G, et al. NetworkAnalyst 3.0: a visual analytics platform for comprehensive gene expression profiling and meta-analysis. Nucleic Acids Res. 2019;47:W234–41.
28. Wagner AH, et al. DGIdb 2.0: mining clinically relevant drug-gene interactions. Nucleic Acids Res. 2016;44:D1036-44.
29. Nuki Y, et al. Elastase-induced intracranial aneurysms in hypertensive mice. Hypertension. 2009;54(6):1337–44.
30. Hosaka K, et al. Modified murine intracranial aneurysm model: aneurysm formation and rupture by elastase and hypertension. J Neurointerv Surg. 2014;6(6):474–9.
31. Zhou D, et al. Identifying pyroptosis- and inflammation-related genes in intracranial aneurysms based on bioinformatics analysis. Biol Res. 2023;56(1):50.
32. McGarry T, et al. Hypoxia, oxidative stress and inflammation. Free Radic Biol Med. 2018;125:15–24.
33. Fan H, et al. CypD induced ROS output promotes intracranial aneurysm formation and rupture by 8-OHdG/NLRP3/MMP9 pathway. Redox Biol. 2023;67:102887.
34. Chen B, et al. Comprehensive analysis of mitochondrial dysfunction and necroptosis in intracranial aneurysms from the perspective of predictive, preventative, and personalized medicine. Apoptosis. 2023;28(9–10):1452–68.
35. Wu A, et al. Integrated analysis identifies the IL6/JAK/STAT signaling pathway and the estrogen response pathway associated with the pathogenesis of intracranial aneurysms. Front Immunol. 2022;13:1046765.
36. Pagano MB, et al. Complement-dependent neutrophil recruitment is critical for the development of elastase-induced abdominal aortic aneurysm. Circulation. 2009;119(13):1805–13.
37. Komi DEA, Kuebler WM. Significance of mast cell formed extracellular traps in microbial defense. Clin Rev Allergy Immunol. 2022;62(1):160–79.
38. Kanematsu Y, et al. Critical roles of macrophages in the formation of intracranial aneurysm. Stroke. 2011;42(1):173–8.
39. Frösen J, et al. Flow-induced, inflammation-mediated arterial wall remodeling in the formation and progression of intracranial aneurysms. Neurosurg Focus. 2019;47(1):E21.
40. Hasan D, et al. Macrophage imbalance (M1 vs. M2) and upregulation of mast cells in wall of ruptured human cerebral aneurysms: preliminary results. J Neuroinflamm. 2012;9:222.
41. Park BS, et al. The structural basis of lipopolysaccharide recognition by the TLR4-MD-2 complex. Nature. 2009;458(7242):1191–5.
42. Bomfim GF, et al. Toll-like receptor 4 inhibition reduces vascular inflammation in spontaneously hypertensive rats. Life Sci. 2015;122:1–7.
43. Moresco EM, LaVine D, Beutler B. Toll-like receptors. Curr Biol. 2011;21(13):R488–93.
44. Zhang Y, et al. Toll-like receptor 4 (TLR4) inhibitors: current research and prospective. Eur J Med Chem. 2022;235:114291.

45. Cusson-Hermance N, et al. Rip1 mediates the Trif-dependent toll-like receptor 3- and 4-induced NF-{kappa}B activation but does not contribute to interferon regulatory factor 3 activation. J Biol Chem. 2005;280(44):36560–6.
46. Nishimura M. Toll-like receptor 4 expression during cerebral aneurysm formation. J Neurosurg. 2013;119(3):825–7.
47. Okada T, Suzuki H. Toll-like receptor 4 as a possible therapeutic target for delayed brain injuries after aneurysmal subarachnoid hemorrhage. Neural Regen Res. 2017;12(2):193–6.
48. Mitsui K, et al. TLR4 (Toll-Like Receptor 4) mediates the development of intracranial aneurysm rupture. Hypertension. 2020;75(2):468–76.
49. Pergola C, et al. Progesterone rapidly down-regulates the biosynthesis of 5-lipoxygenase products in human primary monocytes. Pharmacol Res. 2015;94:42–50.
50. Todur SP, Ashavaid TF. Association of Sp1 tandem repeat polymorphism of ALOX5 with coronary artery disease in Indian subjects. Clin Transl Sci. 2012;5(5):408–11.
51. Li M, et al. Novel diagnostic biomarkers related to oxidative stress and macrophage ferroptosis in atherosclerosis. Oxid Med Cell Longev. 2022;2022:8917947.
52. Mehrabian M, et al. Identification of 5-lipoxygenase as a major gene contributing to atherosclerosis susceptibility in mice. Circ Res. 2002;91(2):120–6.
53. Fan H, et al. miR-566 expression and immune changes in patients with intracranial aneurysm. Int J Clin Exp Pathol. 2020;13(4):685–91.
54. Wang Z, et al. Vascular smooth muscle cells in intracranial aneurysms. Microvasc Res. 2023;149:104554.
55. Shen Y, et al. MicroRNA-disease network analysis repurposes methotrexate for the treatment of abdominal aortic aneurysm in mice. Genomics Proteomics Bioinform. 2023;21(5):1030–42.

Publisher's Note